Research Square

Preprints are preliminary reports that have not undergone peer review.
They should not be considered conclusive, used to inform clinical practice,
or referenced by the media as validated information.

A Physics-aware Melt Pool Feature Integration Framework for Density Prediction and Optimization Strategies Evaluation in Additive Manufacturing

Yunpeng Su
Sichuan university
Yongsheng Zhao
Shijiazhuang Tiedao University
Xiao Liu
Hebei Normal University of Science and Technology
Bin Zhuang
Sichuan university
Renlong Xiong
Sichuan university
Huan Qi
qihuan@scu.edu.cn
Sichuan university

Research Article

Keywords: Physical features, Melt pool features, Density prediction, Optimization strategy evaluation

Posted Date: September 16th, 2026

DOI: https://doi.org/10.21203/rs.3.rs-10897352/v1

License: This work is licensed under a Creative Commons Attribution 4.0 International License.
Read Full License

Additional Declarations: No competing interests reported.

A Physics-aware Melt Pool Feature Integration Framework for Density Prediction and Optimization Strategies Evaluation in Additive Manufacturing

Abstract: With the increasing demand for high-quality additive manufacturing (AM), various process optimization strategies have been developed to improve fabrication performance. However, existing evaluation methods mainly rely on post-fabrication inspection, making it difficult to achieve rapid and quantitative evaluation of optimization strategies. To address this issue, this study takes Directed Energy Deposition (DED) of Cu-12Sn-2Ni alloy as a case study and proposes a density prediction-driven framework for evaluating additive manufacturing optimization strategies. First, to address the degradation of model performance caused by random disturbances in small-sample datasets, a global–local–cluster multi-level noise identification strategy is proposed to achieve hierarchical optimization of data quality. Based on the denoised dataset, a local density prediction model is developed through comparative analysis of different fitting mechanisms and feature ablation experiments. Subsequently, a volume-weighted integration method is introduced to extend local density prediction to overall component density evaluation. The developed framework is further applied to assess different AM optimization strategies. The results show that the proposed multi-level noise identification strategy improves the R^2 of the model by 10.72%. After integrating melt pool features and physical features, the model achieves an R^2 of 0.938, representing a further 6.57% improvement over the model using process parameters. Under different fabrication optimization strategies, the predicted density variation trends are consistent with the experimentally measured results. This study provides a new method for evaluating AM optimization strategies by integrating process parameters and fabrication-state information, enabling quality prediction and process parameter optimization.

Keywords: Physical features; Melt pool features; Density prediction; Optimization strategy evaluation

1. Introduction

AM enables the integrated fabrication of complex structures through layer-by-layer material accumulation. Benefiting from high material utilization efficiency, superior design flexibility, and near-net-shape manufacturing capability, AM has been widely applied in aerospace, energy equipment, and biomedical fields [1-3]. As a critical metal AM technology, DED offers advantages such as high deposition rate, strong dimensional adaptability, and superior capability for component repair and remanufacturing, making it a prominent technique for fabricating high-performance metallic components [4-6]. However, complex heat and mass transfer as well as dynamic coupling effects occur among the laser, powder, and melt pool during DED. These phenomena readily induce defects such as porosity and lack of fusion, compromising component mechanical properties and service reliability [7-9]. To suppress defect formation, researchers have integrated process optimization strategies with DED technology [10, 11]. Nevertheless, existing optimization strategies rely heavily on post-manufacturing destructive testing, which severely impedes their rapid screening and iterative evaluation. Component density serves as a critical indicator of the defect fraction in fabricated components, and the defect suppression efficacy of different optimization strategies can be quantitatively evaluated based on changes in component density. Therefore, establishing a predictive evaluation method that bridges process states with density is important for the screening and optimization of AM processes.

In recent years, machine learning (ML) has gradually emerged as a powerful tool for quality prediction in AM due to its outstanding nonlinear mapping capability and data-driven characteristics [12-14]. Compared with conventional experimental characterization and numerical simulation methods, ML can establish nonlinear relationships between processing conditions and fabrication quality while reducing experimental cycles and computational requirements, thereby providing guidance for process parameter optimization [15].

However, existing ML prediction models predominantly rely on static process parameters, which may limit their predictive accuracy and generalizability across different processing conditions [16]. To address this limitation, physical features have been introduced to characterize the underlying energy transfer and material transport associated with process parameters [17, 18]. Nevertheless, these physical features are still derived from static process parameters and cannot capture the real-time fabrication responses. To further capture the real-time response of the manufacturing process, dynamic

melt pool features have been incorporated to characterize the evolving fabrication state during deposition [19, 20]. As a fundamental processing unit in AM, the melt pool reflects the response to different processing conditions. Variations in melt pool characteristics are closely associated with material consolidation and defect formation, thereby providing information for predicting density [21]. Therefore, integrating process parameters, physical features, and melt pool features provides an effective basis for density prediction and the evaluation of AM optimization strategies.

Furthermore, the performance of ML models is highly dependent on data quality. Due to unavoidable disturbances from equipment vibration and environmental variations, AM datasets inevitably contain random noise [22]. To address noise interference, Pi et al. [23] introduced the DBSCAN (Density - Based Spatial Clustering of Applications with Noise) algorithm to improve the mapping between process parameters and density in AM datasets. However, as a density-based clustering method, DBSCAN primarily identifies anomalies according to local sample density, making it insufficient for identifying global and cluster-level noise in AM datasets [24-26]. In small-sample AM datasets, even a limited number of noisy samples can significantly distort the intrinsic data distribution, leading to reduced prediction accuracy and model robustness [23, 27, 28]. Therefore, developing a multi-level collaborative noise identification strategy is essential for extracting valuable information from AM datasets and providing reliable quantitative evaluation criteria for manufacturing optimization strategies.

Based on the above considerations, this study proposes a density prediction and optimization strategy evaluation framework for AM by integrating physical features and melt pool features, aiming to reduce the influence of noise in small-sample AM datasets and achieve quantitative evaluation of manufacturing optimization strategies. First, considering the characteristics of small-sample AM datasets, a multi-level noise identification strategy is proposed to achieve hierarchical data quality refinement. Second, by integrating process parameters, physical features, and melt pool features, comparative experiments across different model-fitting mechanisms and feature ablation studies are conducted to build a local prediction model, and the overall component density is derived using a volume-weighted approach. Finally, the proposed framework is applied to the DED fabrication of the Cu-12Sn-2Ni alloy. By predicting density variations under different optimization strategies, the effectiveness of these strategies can be quantitatively evaluated without destructive testing.

2. Experimental Design and Data Construction Methodology

2.1 Sample Preparation and Data Acquisition of DED-Processed Cu-12Sn-2Ni Alloy

Cu–12Sn–2Ni powder with a particle size of 53–105 μm was used, and a 45# steel plate with dimensions of 100 mm × 100 mm × 10 mm was employed as the substrate. A Raycus RFL-C2000 fiber laser was used as the heat source and integrated with an HR-SFPFH powder feeding system for synchronized powder delivery. The processing setup was equipped with a D52 straight laser head and a 0610 nozzle, both manufactured by Nanjing Huirui Optics Technology Co., Ltd. The laser spot diameter was fixed at 1 mm. A unidirectional scanning strategy was employed to fabricate Cu–12Sn–2Ni specimens with dimensions of 10 mm × 10 mm × 10 mm.

To investigate the effect of process parameters on quality, an orthogonal experimental design with 6 factors and 5 levels (comprising 100 experiments in total) was established. The selected process parameters included laser power (400 - 1000W), scanning speed (2 - 8 mm/s), powder feeding speed (0.4 - 2.0 rad/min), shielding gas flow rate (3 - 15 NL/min), carrier gas flow rate (3 - 15 NL/min), and overlap ratio (10% - 50%). The experimental workflow and process parameter settings are illustrated in Fig. 1, while photographs of the fabricated specimens are provided in the Supplementary Material.

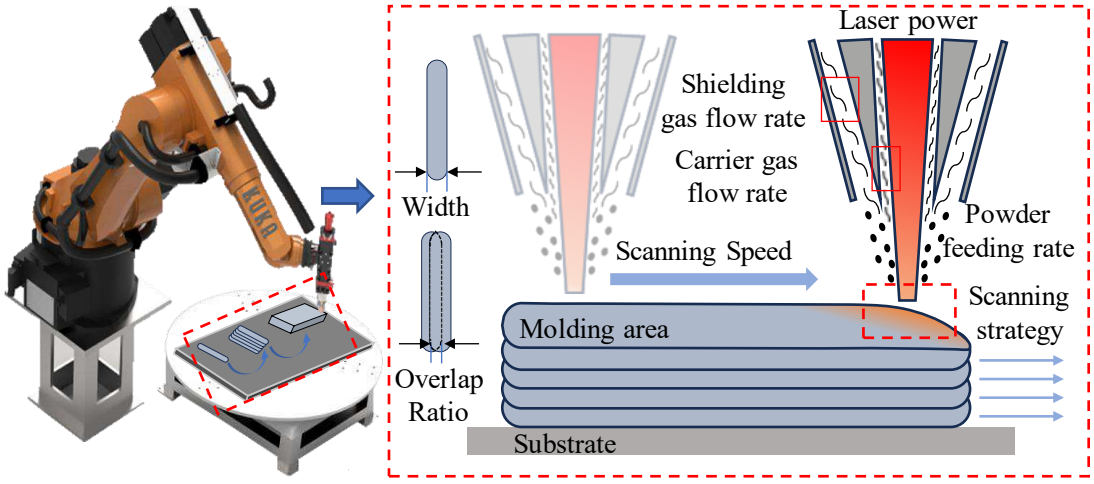


Fig. 1 Schematic diagram of the Cu-12Sn-2Ni specimen fabrication workflow and process parameters

To capture the dynamic evolution of the melt pool, an industrial camera (MER2-041-302GM/P, Daheng Imaging) was employed for monitoring. The camera was coaxially integrated into the laser head, with the frame rate fixed at 50 fps and the exposure time set to 15.628 μs. Melt pool images were continuously captured throughout the deposition process to record the melt pool morphology and its evolution under different processing conditions. A schematic illustration of the melt pool feature acquisition process is shown in Fig. 2.

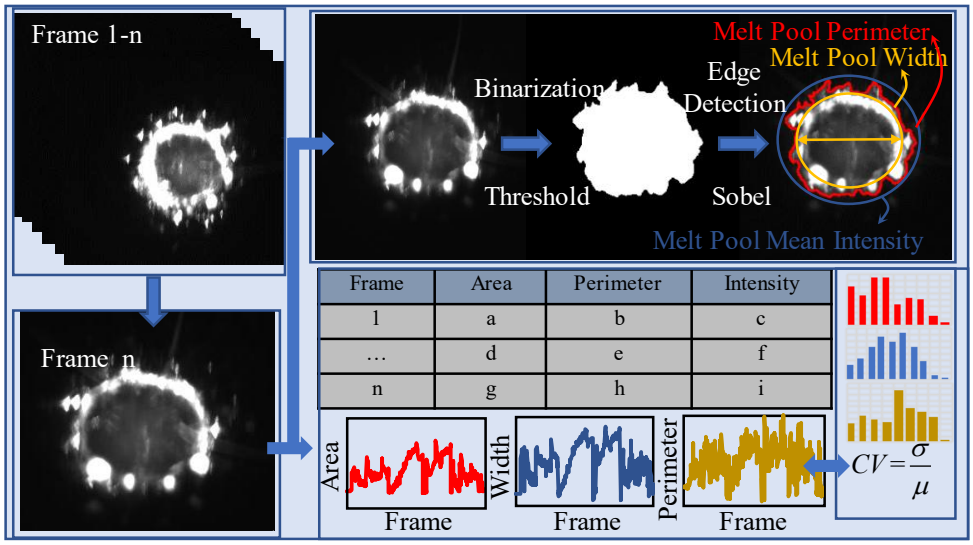


Fig. 2 Schematic illustration of the selected melt pool characteristic parameters

After fabrication, the specimens were separated from the substrate using wire electrical discharge machining (WEDM). The specimen surfaces were polished with abrasive paper until smooth, followed by cleaning with alcohol to remove residual contaminants. The density of the specimens was measured based on Archimedes' principle. An electronic balance was used to measure the mass of each specimen in air and water at 25 °C. The specimen density was calculated according to Eq. (1), while the porosity was calculated using Eq. (2).

$$\rho_{sample}=\frac{m_{air}\cdot\rho_{water}}{\left(m_{air}-m_{water}\right)} \tag{1}$$

$$P=\left(1-\frac{m_{air}\cdot\rho_{water}}{\left(m_{air}-m_{water}\right)\cdot\rho_{\text{Cu-12Sn-2Ni}}}\right)\times 100\% \tag{2}$$

where m_{air} is the mass of the specimen measured in air, m_{water} is the mass of the specimen measured in water, ρ_{water} is the density of deionized water at 25 °C (0.997 g/cm³), ρ_{sample} is the measured density of the specimen, $\rho_{\text{Cu-12Sn-2Ni}}$ is the theoretical density of fully dense Cu-12Sn-2Ni alloy (8.91 g/cm³), and P represents the porosity of the tested specimen.

2.2 Multi-Source Data Feature Construction and Preprocessing

Previous studies have demonstrated that incorporating physical features enhances the capability of ML models to characterize the manufacturing processes [29]. To further improve predictive accuracy, physical features, including linear energy density, powder-specific energy, gas flow ratio, areal energy density, and volumetric energy density, were incorporated into the dataset. The process

parameters, physical features, and melt pool features were used as the input variables, while density was used as the output variable.

Considering the differences in magnitude among the input features, data preprocessing was performed prior to model training. Since the process parameters were derived from an orthogonal experimental design, Min–Max scaling was applied for normalization to retain the relative relationships among the samples, as expressed in Eq. (3). In contrast to the process parameters, melt pool features and density values contain outliers. Therefore, the melt pool features and density were standardized using the Power Transformer to reduce the influence of extreme values while preserving the statistical characteristics of the data.

$$x_{norm} = \frac{x_i - x_{\min}}{x_{\max} - x_{\min}} \tag{3}$$

where x_{norm} represents the normalized feature value, x_i represents the original feature value, $x_{\max}$ represents the maximum value of the original feature, and $x_{\min}$ represents the minimum value of the original feature.

2.3 Evaluation Metrics for Density Prediction Models

To evaluate the predictive performance of different models under small-sample conditions, the mean absolute error (MAE), root mean square error (RMSE), and coefficient of determination (R^2) were used to evaluate model performance. The calculation formulas for these metrics are given in Eqs. (4) – (6).

$$MAE = \frac{1}{n}\sum_{i=1}^{n}\left|y_{i-measure} - y_{i-predict}\right| \tag{4}$$

$$RMSE = \sqrt{\sum_{i=1}^{n}\frac{\left(y_{i-measure} - y_{i-predict}\right)^2}{n}} \tag{5}$$

$$R^2 = 1 - \frac{\sum_{i=1}^{n}(y_{i,measure} - y_{i,predict})^2}{\sum_{i=1}^{n}(y_{i,measure} - \overline{y_i})} \tag{6}$$

where $y_{i-measure}$ is the measured density value of the i-th sample, $y_{i-predict}$ is the predicted density value of the i-th sample, $\overline{y_i}$ is the average density of the sample, and n represents the total number of the sample.

3. Construction of Density Prediction Framework Integrating Physical and Melt Pool Features

3.1 Multi-Level Collaborative Noise Identification for Small-Sample AM Data

Affected by the combined influence of process design and random disturbances, noise in AM processes often exhibits a multi-scale distribution. In small-sample datasets, even a few noisy data points can degrade the predictive performance of the ML model. Therefore, this framework establishes a global–local–cluster collaborative noise identification strategy to progressively filter out noise and construct a higher-quality small-sample dataset.

From the perspective of global statistical distribution, Mahalanobis Distance (MD) determines whether a sample deviates from the overall data structure based on the mean vector and covariance matrix of the dataset, which exhibits good applicability for uniformly distributed sample spaces generated via orthogonal experimental designs [30]. However, MD is insensitive to noise distributed in local regions. In AM processes, transient disturbances can induce local anomalies, which may not show significant deviations at the global scale. Therefore, MD is insufficient for identifying local noise. To address this limitation, the DBSCAN algorithm is introduced to detect local noise at the structural level by specifying the neighborhood radius and minimum number of samples, thereby classifying isolated points as noise.

After sequentially removing global and local noise, the dataset is partitioned into multiple clusters. Although samples within the same cluster exhibit similar characteristics, abnormal samples existing within high-density clusters still require further identification [31, 32]. When a cluster contains more than five samples, the local density distribution within the cluster exhibits statistical stability [33]. Therefore, the density-based Local Outlier Factor (LOF) algorithm is employed for intra-cluster noise identification [34, 35]. When the number of samples within a cluster is limited (sample size ≤ 5), the reliability of local density estimation decreases [33, 36, 37]. In this case, the K-nearest neighbor (KNN) algorithm is adopted to identify noise samples based on the deviation of distances between samples and their neighboring points [33, 36, 37].

To achieve consistent evaluation across different clusters, after completing noise identification within all clusters, the distance-based metrics of each cluster are standardized using Z-score normalization, from which relative quantiles are derived. Samples are then uniformly ranked based on the quantiles, and samples with high quantile values are labeled as potential noise points. When

the samples exhibit identical quantile values, decisions are made based on their corresponding Z-scores.

Through hierarchical noise identification from global, local, and cluster levels, a more reliable dataset is constructed for subsequent density prediction. The overall schematic diagram of the multi-level noise identification framework is shown in Fig. 3. The complete identification strategy is illustrated in Fig. 3(a), while the intra-cluster noise identification strategy is presented in Fig. 3(b).

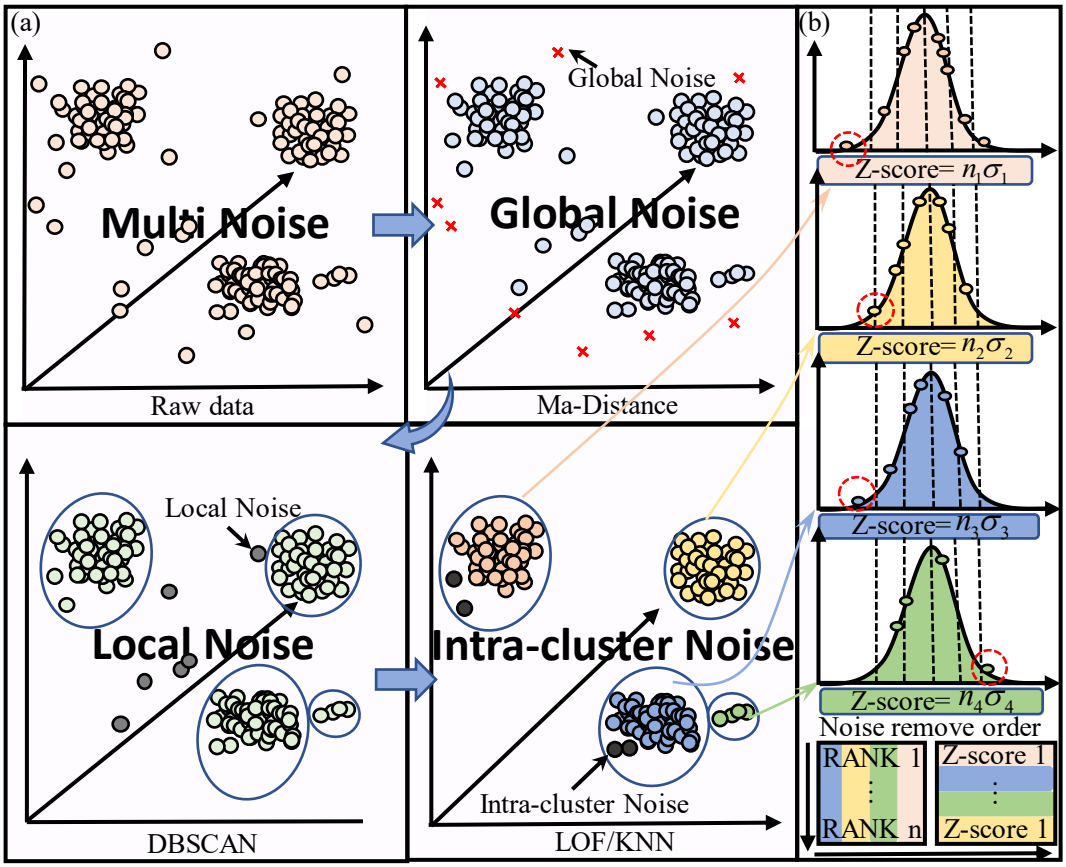


Fig. 3. Schematic illustration of the multi-level noise identification strategy: (a) multi-level noise identification procedure; (b) intra-cluster noise identification procedure

After removing the identified noise samples, the density prediction model was retrained using the denoised dataset. To evaluate the effectiveness of the proposed multi-level collaborative noise identification strategy, K-means, DBSCAN, and MD were selected as comparative methods, and the number of removed noise samples was progressively increased from 1 to 10.

3.2 Selection of ML Fitting Mechanisms and Construction of the Density Prediction Model for Small-Sample Data

After optimizing the dataset quality, a density prediction model customized for small-sample AM

datasets was constructed. During the DED process, density exhibits highly nonlinear relationships with process parameters and melt pool features. The dataset in this study comprises 100 experimental samples, with input features illustrated in Fig. 4(a), representing a typical small-sample, multi-variable dataset. Therefore, a density prediction model with both strong fitting capability and generalization performance is required under limited data conditions [38, 39].

Within a stable DED processing window, density generally exhibits a continuous and smooth response to energy input. Therefore, ML models with explicit regularization or function-space constraints, including Support Vector Regression (SVR), Gaussian Process Regression (GPR), and Ridge Regression (Ridge), were introduced. These models can regulate the variation scale and smoothness of the fitted function in the input space through kernel functions and hyperparameters, thereby improving predictive robustness under small-sample conditions [40, 41].

Considering the localized response characteristics of density across different DED processing conditions, Random Forest (RF) and Extreme Gradient Boosting (XGBoost) models based on spatial partitioning and ensemble learning were employed. By recursively partitioning the input space via tree structures, these models effectively capture complex nonlinear interactions among multiple parameters under small-sample conditions, making them suited for capturing localized nonlinear variations in density across different process conditions and melt pool states [42, 43].

Furthermore, to further characterize the nonlinear mapping between the input parameters and density, an artificial neural network (ANN) model with multiple fully connected layers was incorporated, capturing the continuous density evolution induced by multi-parameter coupling [44-46].

In summary, the above models represent three distinct fitting mechanisms: functional regularization and smoothness constraints, recursive spatial partitioning, and nonlinear function approximation, as schematically illustrated in Fig. 4(b). By comparing the predictive performance of the models, the applicability of different data-mapping mechanisms can be evaluated. Meanwhile, the effectiveness of the noise filtering strategies described in Section 3.1 can be further verified, thereby providing a basis for constructing a density prediction model suitable for small-sample AM data.

After selecting the optimal fitting mechanism, identifying the optimal input feature combination is essential for achieving the best predictive performance. Preliminary analysis indicated that not all melt pool features and physics features contribute positively to density prediction. To construct the

optimal density prediction model, ablation studies were conducted by systematically combining process parameters, physical features, and melt pool features.

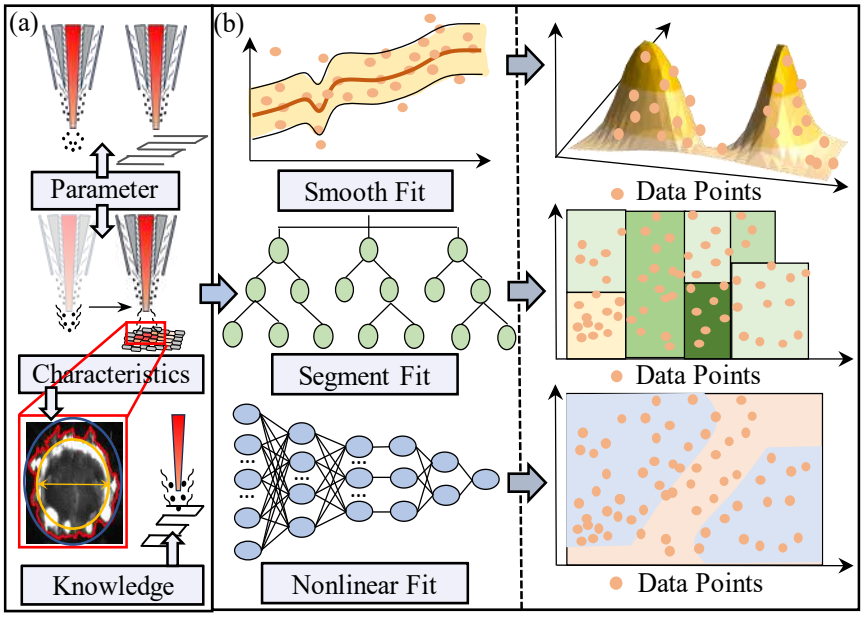


Fig. 4. Schematic illustration of the ML model fitting mechanisms

3.3 Overall Density Prediction Based on Volume-Weighted Integration

The AM process follows a point-to-line, line-to-surface, and surface-to-solid layer-by-layer deposition mechanism. The instantaneous process parameters and melt pool states during deposition are associated with local deposition locations, while the overall density of a part is determined by the spatial accumulation of density states across the local deposition points. Therefore, capturing instantaneous melt pool states and process parameter information enables the density prediction of local forming points. By performing a volume-weighted aggregation of the predicted local density values of all deposition points across the entire spatial domain, the overall density of the fabricated part can be evaluated. This approach is schematically illustrated in Fig. 5(a)–(b), with the corresponding calculation procedure defined in Eq. (7).

$$Density_{total} = \frac{\sum_{i=1}^{n} Density_i * d_i * h_i * L_i}{\sum_{i=1}^{n} d_i * h_i * L_i} \tag{7}$$

where $Density_{total}$ represents the overall density of the fabricated part, $Density_i$ represents the density of a local deposition unit, d_i represents the width of the deposition unit, and h_i represents

the height of the deposition unit. The density, width, and height of the deposition unit are all obtained from the corresponding ML models, which are constructed following the same modeling framework as the density prediction model. L_i represents the length of the deposition unit, which can be obtained from the laser head coordinates. n represents the total number of deposition units, which is calculated according to Eq. (8).

$$n = \frac{t_{total}}{t_i} \tag{8}$$

where t_{total} represents the total fabrication time, and t_i represents the sampling interval.

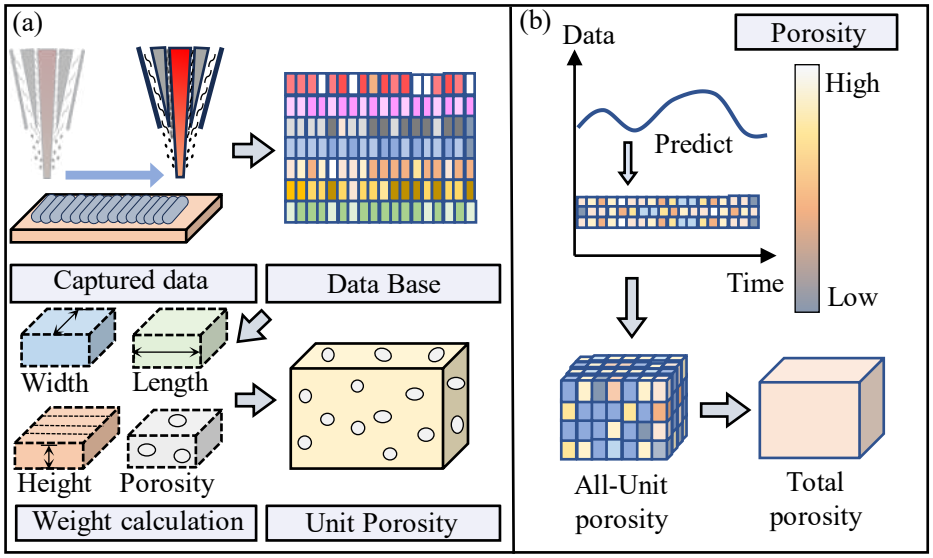


Fig. 5 Schematic illustration of the density prediction: (a) local deposition point density prediction; (b) overall component density prediction based on volume-weighted integration

4. Density Prediction and Optimization Strategy Evaluation of Cu–12Sn–2Ni

4.1 Construction of the Cu–12Sn–2Ni Density Prediction Model Based on Multi-Level Noise Identification

To ensure reliable model evaluation, the dataset was partitioned into training and testing sets at an 80:20 ratio, followed by 10-fold nested cross-validation. The prediction results corresponding to different noise identification strategies and varying numbers of removed noisy samples are illustrated in Fig. 6(a), while the R^2 on the testing set under different combinations of physical features and melt pool features is presented in Fig. 7. The results demonstrate that the proposed global–local–cluster multi collaborative noise identification strategy achieved the strongest generalization capability in the

testing set, with a maximum improvement of 10.72% in R^2 compared to the model without noise treatment. When VED (volumetric energy density) and GCR (gas flow ratio) were incorporated as physical features, the mean melt pool intensity and coefficient of variation of melt pool width were selected as melt pool features, with 8 global and 1 local noisy points removed, the GPR model achieved the highest R^2 value of 0.826 on the testing set, representing a 6.57% improvement over the model using process parameters as inputs.

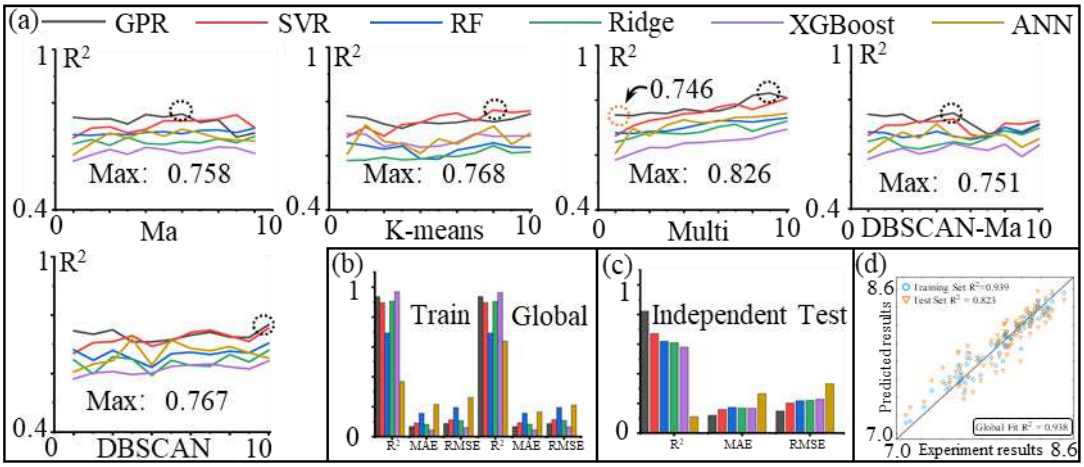


Fig. 6 Performance summary of the density prediction model: (a) variation in R^2 with different noise identification strategies and numbers of removed noise samples; (b) performance metrics of the optimal model on the training set and complete noise-filtered dataset; (c) performance metrics of the optimal model on the independent testing set; (d) predicted values and actual density values of the optimal model

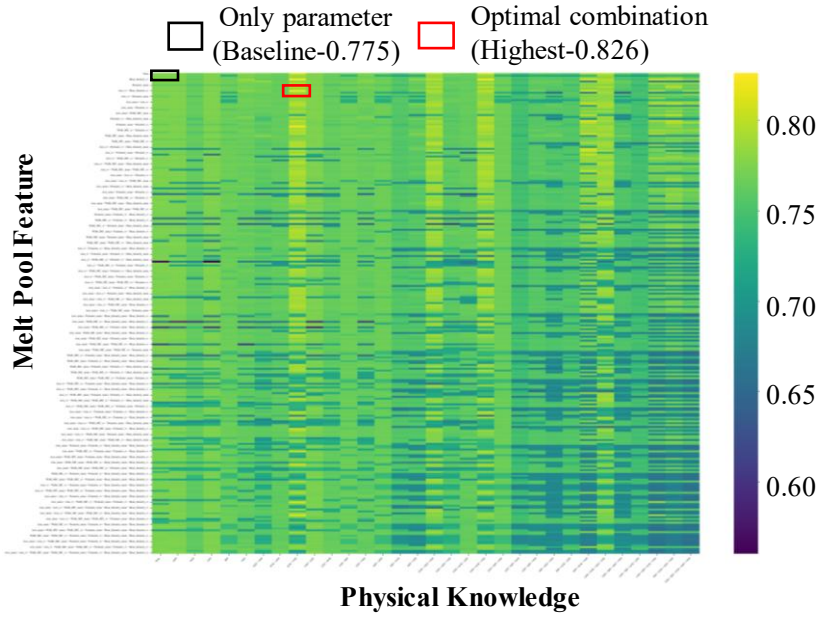


Fig. 7. R^2 values obtained using different combinations of physical features and melt pool features

After determining the optimal model and input feature combination, all remaining noise-filtered samples were used to train the density prediction model. The R^2, MAE, and RMSE metrics of the model on the training set, testing set, and entire dataset are presented in Fig. 6(b)–(c), with an R^2 of 0.938 for the entire dataset. The comparison between the predicted and actual values is shown in Fig. 6(d).

4.2 Construction of the Cu–12Sn–2Ni Process Parameter Space Based on the Density Prediction Model

The density of the part is jointly determined by the process parameters and melt pool behavior. In the construction of the density prediction model, the input variables comprised three categories: process parameters, physical features, and melt pool features. In this study, the physical features were derived from the process parameters, whereas the melt pool features did not have predefined ranges. In contrast, the equipment constraints and material characteristics defined the feasible process window. To ensure the practicality of the input data, the process parameter space was constructed by systematically enumerating combinations of the process parameters, as schematically illustrated in Fig. 8.

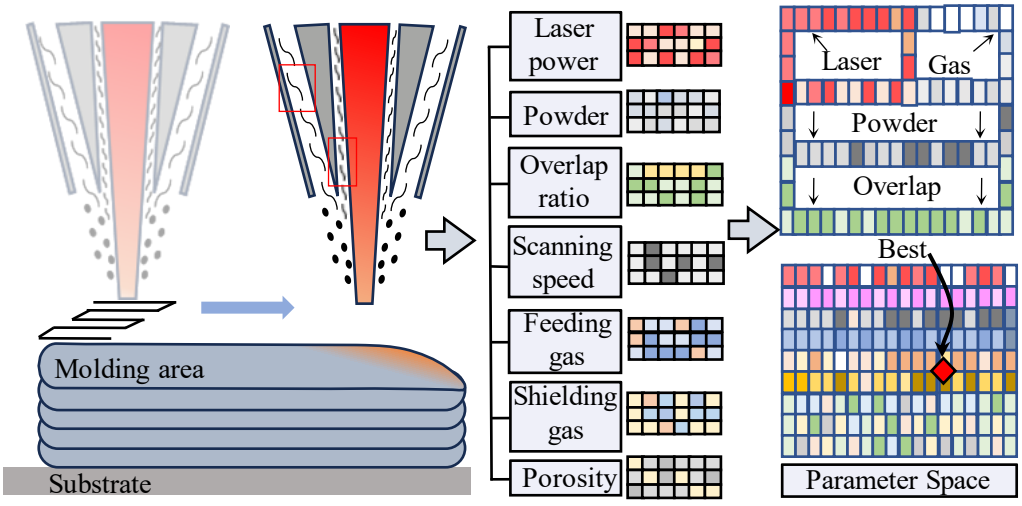


Fig. 8. Schematic illustration of the process parameter space construction

The parameter combinations were enumerated using a step size of 10 W for laser power (400–1000 W), 0.1 rad/min for powder feeding speed (0.4–2.0 rad/min), 0.1 mm/s for scanning speed (2–8 mm/s), 1 NL/min for shielding gas flow rate (3–15 NL/min), 1 NL/min for powder carrier gas flow rate (3–15 NL/min), and 5% for overlap ratio (10%–50%). The corresponding density predictions were obtained for each parameter combination to construct the process parameter space.

The parameter space indicated that the highest predicted density for the Cu–12Sn–2Ni specimens could be obtained at a laser power of 1000 W, a powder feeding speed of 0.4 rad/min, a scanning speed of 5.5 mm/s, a shielding gas flow rate of 15 NL/min, a powder carrier gas flow rate of 4 NL/min, and an overlap ratio of 50%. The predicted density of the sample was 8.92 g/cm³, while the measured density was 8.89 g/cm³.

To quantitatively evaluate the accuracy of the density prediction model, the predicted density values within the parameter space were ranked in ascending order and divided into five equal intervals. One process parameter combination was randomly selected from each interval for experimental fabrication (labeled as Samples 1–5), and the corresponding melt pool features and process parameters during deposition were recorded.

The predicted and measured density results of the five samples are presented in Table 1, and the corresponding specimens are shown in Fig. 9. The results show that the density prediction model using process parameters as inputs achieved a mean relative error of 1.9288%. After incorporating physical and melt pool features, the mean relative error decreased to 0.9699%. When volume-weighted integration was further incorporated, the prediction error was reduced to 0.9527%.

Table 1. Predicted and measured densities of Samples 1–5

No.	Laser power (W)/ Feeding speed (rad/min)/ Scanning speed (mm/s)/ Shield gas flow (NL/min)/ Feeding gas (NL/min)/ Overlap ratio (%)	Density Prediction by Parameter / Parameter & Melt Pool features & Physical features (g/cm³)	Unit weight Density Prediction by Parameter / Parameter & Melt Pool features & Physical features (g/cm3)	Real density (g/cm3)
1	530/ 0.6/ 4.0/ 9.0/ 12.0/ 50.0	8.7618/8.7049	8.7618/8.7044	8.6198
2	990/ 0.8/ 7.2/ 12.0/ 15.0/ 25.0	8.5728/8.3898	8.5728/8.3847	8.2921
3	940/ 1.8/ 6.4/ 3.0/ 12.0/ 40.0	8.3267/8.4455	8.3267/8.4473	8.4537
4	910/ 1.6/ 5.6/ 5.0/ 9.0/ 45.0	8.2591/8.2888	8.2591/8.2909	8.3405
5	730/ 1.4/ 4.0/ 4.0/ 9.0/ 10.0	8.0644/8.0780	8.0644/8.0757	8.2401

Pairwise combinations of laser power, scanning speed, powder feeding speed, powder carrier gas flow rate, and overlap ratio were assigned to the X and Y axes, while the remaining process parameters

were fixed at their optimal values. The corresponding density prediction results were visualized, with representative results shown in Fig. 10.

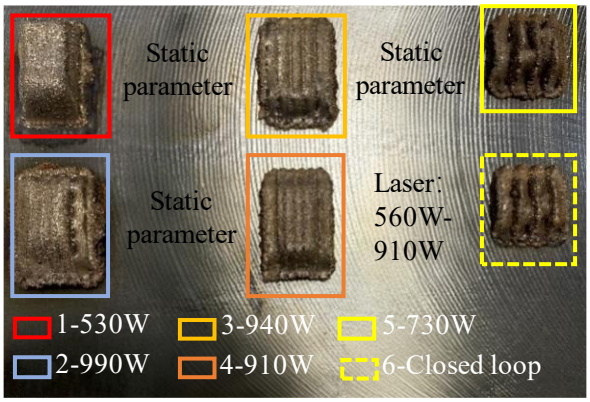


Fig. 9 Cu-12Sn-2Ni specimens (Samples 1–6) fabricated by DED

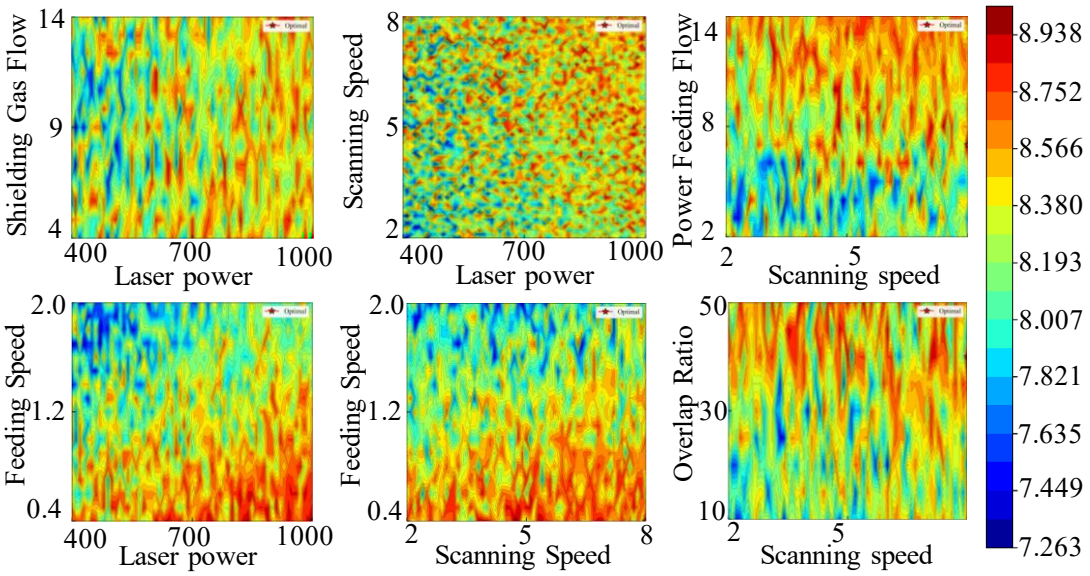


Fig. 10 Process parameter space maps for the Cu-12Sn-2Ni alloy

4.3 Evaluation of Cu–12Sn–2Ni Manufacturing Optimization Strategies Based on Density Prediction

To further validate the density prediction capability of the model integrating melt pool features and physical features, specimens were fabricated using different optimization strategies, and the densities of the specimens were predicted and experimentally measured.

Closed-loop feedback was applied to Sample 5, which exhibited the lowest density. The density under static process parameters was predicted, and the density fluctuation range was determined by the model prediction error. Based on the density fluctuation range, the corresponding laser power control range was obtained by inversely mapping the density fluctuation range onto the process parameter space. The procedure for determining the control parameter range is illustrated in Fig. 11.

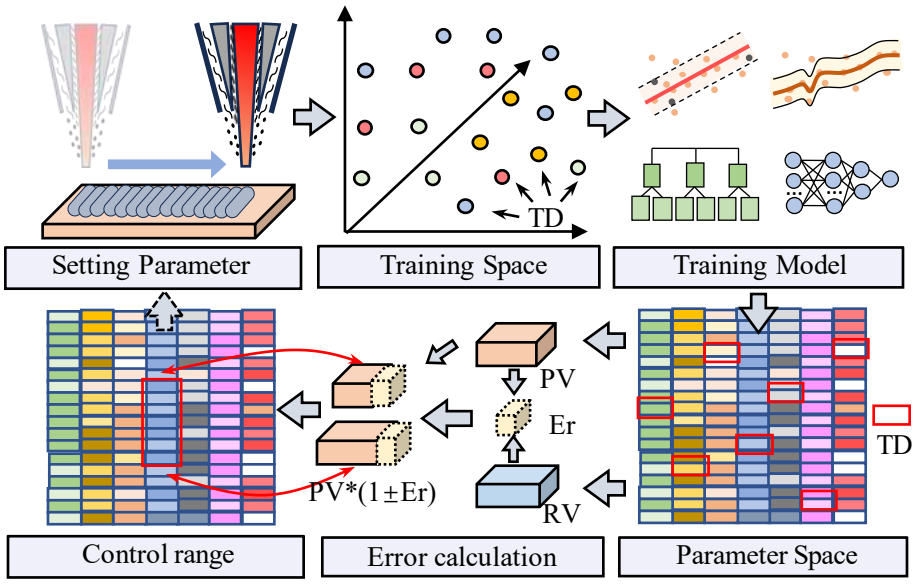


Fig. 11. Procedure for determining the control parameter range

Keeping all other process parameters identical to Sample 5, closed-loop feedback control was implemented using a laser power control range of 560–910 W, and the resulting specimen was designated as Sample 6. The measured and predicted density results are presented in Table 2, and the fabricated specimen is shown in Fig. 9. The results show that the density of Sample 6 increased by 2.6262% compared to Sample 5. The prediction error was 5.2226% when process parameters were used as inputs, which decreased to 4.7962% after incorporating melt pool features and physical features. With further integration of volume-weighted information, the prediction error was reduced to 4.7746%.

Table 2. Predicted and measured densities of Samples 6–14 under different manufacturing optimization strategies

No.	Laser power (W)/ Feeding speed (rad/min)/ Scanning speed (mm/s)/ Shield gas flow (NL/min)/ Powder feeding flow (NL/min)/ Overlap ratio (%)	Optimization strategy	Density Prediction by Parameter / Parameter & Melt Pool features & Physical features (g/cm^3)	Unit weight Density Prediction by Parameter / Parameter & Melt Pool features & Physical features (g/cm3)	Real density (g/cm3)
6	730/ 1.4/ 4.0/ 4.0/ 9.0/ 10.0	Closed-loop feedback	8.0149/8.0509	8.0184/8.0527	8.4565
7	450/ 0.6/ 4.0/ 9.0/ 12.0/ 50.0	\	8.7431/8.6905	8.7431/8.6882	8.6221

Table 2. (continued)

No.	Laser power (W)/ Feeding speed (rad/min)/ Scanning speed (mm/s)/ Shield gas flow (NL/min)/ Powder feeding flow (NL/min)/ Overlap ratio (%)	Optimization strategy	Density Prediction by Parameter / Parameter & Melt Pool features & Physical features (g/cm^3)	Unit weight Density Prediction by Parameter / Parameter & Melt Pool features & Physical features (g/cm3)	Real density (g/cm3)
8	550/ 0.6/ 4.0/ 9.0/ 12.0/ 50.0	\	8.7618/8.7088	8.7618/8.7069	8.6199
9	650/ 0.6/ 4.0/ 9.0/ 12.0/ 50.0	\	8.7841/8.7284	8.7841/8.7282	8.6212
10	750/ 0.6/ 4.0/ 9.0/ 12.0/ 50.0	\	8.7971/8.7434	8.7971/8.7433	8.6126
11	450/ 0.6/ 4.0/ 9.0/ 12.0/ 50.0	Ultrasonic field-20Khz-20um	8.7431/8.6874	8.7431/8.6863	8.6176
12	550/ 0.6/ 4.0/ 9.0/ 12.0/ 50.0	Multi-Field：Ultrasonic - 20Khz - 20um & Magnetic - 50Mt Thermal - 200℃	8.7618/8.7133	8.7618/8.7101	8.6200
13	650/ 0.6/ 4.0/ 9.0/ 12.0/ 50.0	Magnetic field-50mT	8.7841/8.7281	8.7841/8.7280	8.6221
14	750/ 0.6/ 4.0/ 9.0/ 12.0/ 50.0	Thermal field-200℃	8.7971/8.7443	8.7971/8.7441	8.6165

To evaluate the effect of external-field-assisted fabrication on Cu–12Sn–2Ni specimens, the process parameter combination of Sample 1 was selected as the reference condition. Based on the model prediction error, the laser power was set to 450 W, 650 W, and 750 W, while keeping all other process parameters identical to Sample 1. Samples 11,13, and 14 were fabricated under a 20 kHz/20 μm ultrasonic vibration field, a 50 mT magnetic field, and a 200 °C thermal field, respectively. In addition, Sample 12 was fabricated at a laser power of 550 W with all three fields applied simultaneously. The experimental equipment and model evaluation workflow are illustrated in Fig. 12, and the fabricated specimens are shown in Fig. 13.

The results show that the externally applied thermal field suppressed pore formation, resulting in a 0.0451% increase in density relative to Sample 10. The magnetic field had a negligible effect on pore formation, with a density variation of only 0.0104% relative to Sample 7. In contrast, ultrasonic vibration had a negative effect on the fabrication of Cu–12Sn–2Ni, resulting in a density decrease of 0.0520% relative to Sample 9. Under the different external-field-assisted fabrication conditions, the mean relative error was 1.7693% when process parameters were used as inputs, which decreased to 1.1514% after incorporating melt pool features and physical features. With further integration of volume-weighted information, the mean relative error was reduced to 1.1385%. The predicted trends in density variation under different manufacturing optimization techniques were consistent with the experimentally measured results.

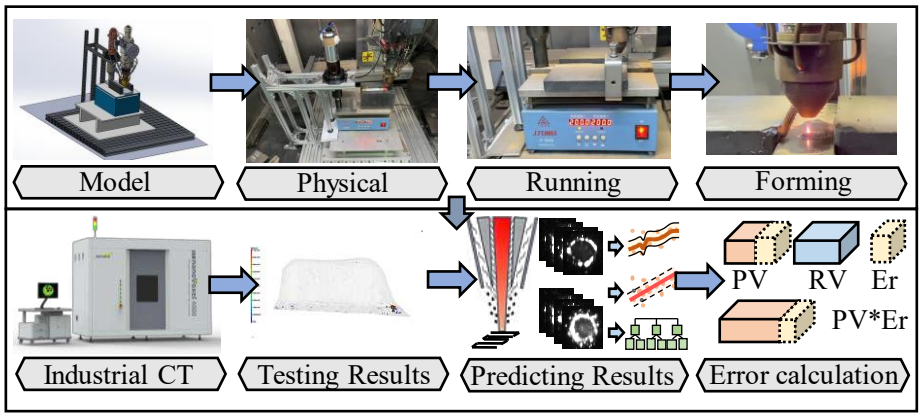


Fig. 12. Workflow for evaluating manufacturing optimization strategies

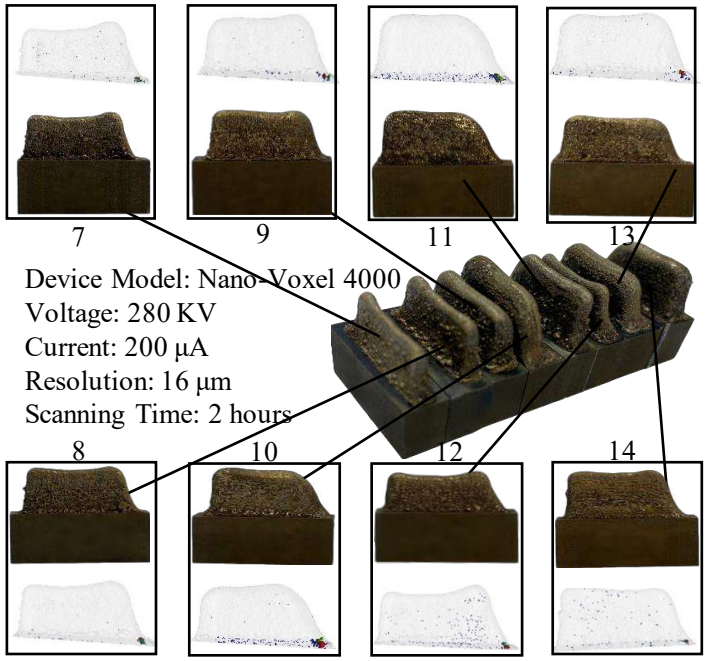


Fig. 13. Cu–12Sn–2Ni specimens (Samples 7–14) fabricated under different manufacturing optimization strategies

5. Conclusions and Outlook

To address the random noise present in small-sample AM datasets, a global–local–cluster collaborative noise identification strategy was proposed to achieve hierarchical data quality optimization. Compared with the model without noise reduction, the optimized dataset achieved a 10.72% improvement in R^2. On this basis, process parameters, physical features, and dynamic melt pool features were integrated to construct a density prediction model. Through ablation experiments, the optimal input feature space was identified. Compared with the prediction model using process parameters, incorporating melt pool features and physical features increased the R^2 by 6.57%, while the mean relative error under static process parameters decreased from 1.9288% to 0.9699%. Furthermore, the proposed model was applied to the evaluation of manufacturing optimization strategies, including closed-loop feedback control and external-field-assisted fabrication. The predicted trends in density variation were consistent with the experimentally measured results, with a mean relative error of 1.1385% across different external-field-assisted fabrication conditions. These results validate the efficacy of the proposed framework for density prediction and process optimization evaluation.

However, the prediction model developed in this study primarily focuses on melt pool features, process parameters, and physical features, while the temperature field during fabrication has not yet been fully incorporated. Future work could incorporate infrared thermography to expand the multimodal input space, thereby enhancing the model's generalizability under complex operating conditions and across different equipment platforms. In addition, the proposed overall density prediction method is based on volume-weighted aggregation of local fabrication states and does not fully account for the spatial correlations and temporal accumulation effects during continuous deposition. Future research could incorporate spatiotemporal deep learning models or multi-physics coupling methods to further improve density prediction for complex components. Moreover, the proposed framework has currently been validated only for the DED fabrication of Cu–12Sn–2Ni alloy, and its applicability to different material systems and AM processes remains to be further evaluated. Future efforts will focus on cross-material and cross-process validations to establish a generalized density prediction and process evaluation framework.

Funding

This work was supported by Sichuan Science and Technology Program (2025ZDZX0055), Sichuan Provincial Youth Science and Technology Foundation (2025ZNSFSC0841), Nuclear Power Innovation Fund: Sichuan University–Institute of Nuclear Power Joint Innovation Fund (SCU&NPIC-LHCX-202505).

Declaration of Competing Interest

The authors declare that they have no known competing financial interests or personal relationships that could have appeared to influence the work reported in this paper.

Data availability statement

The data presented in this study are available upon reasonable request from the corresponding author.

Reference

[1] D.M. Wirth, C.C. Li, J.K. Pokorski, H.K. Taylor, M. Shusteff, Fundamental scaling relationships in additive manufacturing and their implications for future manufacturing and bio-manufacturing systems, Additive Manufacturing 84 (2024) 104081. https://doi.org/10.1016/j.addma.2024.104081.

[2] T.D. Ngo, A. Kashani, G. Imbalzano, K.T. Nguyen, D. Hui, Additive manufacturing (3D printing): A review of materials, methods, applications and challenges, Composites Part B: Engineering 143 (2018) 172-196. https://doi.org/10.1016/j.compositesb.2018.02.012.

[3] D. Herzog, V. Seyda, E. Wycisk, C. Emmelmann, Additive manufacturing of metals, Acta Materialia 117 (2016) 371-392. https://doi.org/10.1016/j.actamat.2016.07.019.

[4] M. Peron, A.M. Coruzzolo, R. Basten, N. Knofius, F. Lolli, F. Sgarbossa, Choosing between additive and conventional manufacturing of spare parts: On the impact of failure rate uncertainties and the tools to reduce them, International Journal of Production Economics 278 (2024) 109438. https://doi.org/10.1016/j.ijpe.2024.109438.

[5] K. Kim, K. Park, H.W. Jeon, G.E. Kremer, Design complexity based flexible order dispatching for additive manufacturing production, International Journal of Production Economics 274 (2024) 109307. https://doi.org/10.1016/j.ijpe.2024.109307.

[6] Y. Ji, M. Kim, B. Lee, Mass Customization Through Additive Manufacturing: Review of Technologies, Applications, and Scalability Challenges, International Journal of Precision Engineering and Manufacturing-Green Technology (2026) 1-28. https://doi.org/10.1007/s40684-026-00856-y.

[7] S. Singamneni, L. Yifan, A. Hewitt, R. Chalk, W. Thomas, D. Jordison, Additive manufacturing for the aircraft industry: a review, J. Aeronaut. Aerosp. Eng 8(1) (2019) 351-371. https://doi.org/10.4172/2329-6542.1000214.

[8] L. Smith, O. Scott-Emuakpor, J. Gockel, D. Celli, P. Johnson, Vibration bending fatigue analysis of Ti-6Al-4V airfoil blades repaired using additive manufacturing, Fatigue & Fracture of Engineering Materials & Structures 47(4) (2024) 1417-1430. https://doi.org/10.1111/ffe.14234.

[9] T.F. Babuska, B.A. Krick, D.F. Susan, A.B. Kustas, Comparison of powder bed fusion and directed energy deposition for tailoring mechanical properties of traditionally brittle alloys, Manufacturing Letters 28 (2021) 30-34. https://doi.org/10.1016/j.mfglet.2021.02.003.

[10] H. Yi, T. Lang, J. Si, Y. Chi, H. Cao, Y. Huang, High-performance manufacturing of metal components via multi-field

assisted wire-arc directed energy deposition, Journal of Manufacturing Processes 143 (2025) 234-276. https://doi.org/10.1016/j.jmapro.2025.04.016.
[11] M. Rahmani Dehaghani, A. Sahraeidolatkhaneh, M. Nilsen, F. Sikström, P. Sajadi, Y. Tang, G.G. Wang, System identification and closed-loop control of laser hot-wire directed energy deposition using the parameter-signature-quality modeling scheme, Journal of Manufacturing Processes 112 (2024) 1-13. https://doi.org/10.1016/j.jmapro.2024.01.029.
[12] T. DebRoy, H.L. Wei, J.S. Zuback, T. Mukherjee, J.W. Elmer, J.O. Milewski, A.M. Beese, A. Wilson-Heid, A. De, W. Zhang, Additive manufacturing of metallic components–process, structure and properties, Progress in materials science 92 (2018) 112-224. https://doi.org/10.1016/j.pmatsci.2017.10.001.
[13] S.A. Khairallah, A.T. Anderson, A. Rubenchik, W.E. King, Laser powder-bed fusion additive manufacturing: Physics of complex melt flow and formation mechanisms of pores, spatter, and denudation zones, Acta Materialia 108 (2016) 36-45. https://doi.org/10.1016/j.actamat.2016.02.014.
[14] D. Weisz-Patrault, Fast simulation of temperature and phase transitions in directed energy deposition additive manufacturing, Additive Manufacturing 31 (2020) 100990. https://doi.org/10.1016/j.addma.2019.100990.
[15] A. Yu, Y. Pan, F. Wan, G. Sun, J. Zhang, X. Lu, Rapid accomplishment of cost-effective and macro-defect-free LPBF-processed Ti parts based on deep data augmentation, Journal of Manufacturing Processes 120 (2024) 1023-1034. https://doi.org/10.1016/j.jmapro.2024.05.003.
[16] R. Liu, S. Liu, X. Zhang, A physics-informed machine learning model for porosity analysis in laser powder bed fusion additive manufacturing, The International Journal of Advanced Manufacturing Technology 113(7) (2021) 1943-1958. https://doi.org/10.1007/s00170-021-06640-3.
[17] Z. Smoqi, A. Gaikwad, B. Bevans, M.H. Kobir, J. Craig, A. Abul-Haj, A. Peralta, P. Rao, Monitoring and prediction of porosity in laser powder bed fusion using physics-informed meltpool signatures and machine learning, Journal of Materials Processing Technology 304 (2022) 117550. https://doi.org/10.1016/j.jmatprotec.2022.117550
[18] M. Faegh, S. Ghungrad, J.P. Oliveira, P. Rao, A. Haghighi, A review on physics-informed machine learning for process-structure-property modeling in additive manufacturing, Journal of Manufacturing Processes 133 (2025) 524-555. https://doi.org/10.1016/j.jmapro.2024.11.066.
[19] R. Alfattani, M.M. Hotami, Digital twin–driven multiscale modelling for real-time defect prediction in metal additive manufacturing, Scientific Reports (2026). https://doi.org/10.1038/s41598-026-58348-7.
[20] M.M.a. Imran, J. Kang, Y. Kim, G. Jung, T. Park, A. Che Idris, J.-H. Suh, L.C. De Silva, P.E. Abas, Y.B. Kim, Prediction of melt pool height based on the spatiotemporal adjacency features in laser metal deposition using machine learning, Progress in Additive Manufacturing 10(10) (2025) 7471-7500. https://doi.org/10.1007/s40964-025-01047-y.
[21] L. Zheng, Q. Zhang, H. Cao, W. Wu, H. Ma, X. Ding, J. Yang, X. Duan, S. Fan, Melt pool boundary extraction and its width prediction from infrared images in selective laser melting, Materials & Design 183 (2019) 108110. https://doi.org/10.1016/j.matdes.2019.108110.
[22] B. Ahmmed, E.G. Rau, M.K. Mudunuru, S. Karra, J.R. Tempelman, A.J. Wachtor, J.-B. Forien, G.M. Guss, N.P. Calta, P.J. DePond, Deep learning with mixup augmentation for improved pore detection during additive manufacturing, Scientific Reports 14(1) (2024) 13365. https://doi.org/10.1038/s41598-024-63288-1.
[23] Q. Pi, R. Li, B. Han, K. Yang, Y. Hu, Y. Shi, H. Qi, W. Li, K. Bi, G. Sun, Predicting the porosity of as-built additive manufactured samples based on machine learning method for small datasets, Optics & Laser Technology 177 (2024) 111203. https://doi.org/10.1016/j.optlastec.2024.111203.
[24] J. Kim, H. Lee, Y.M. Ko, Constrained density-based spatial clustering of applications with noise (DBSCAN) using hyperparameter optimization, Knowledge-Based Systems 303 (2024) 112436. https://doi.org/10.1016/j.knosys.2024.112436.
[25] K. Giri, T.K. Biswas, P. Sarkar, ECR-DBSCAN: An improved DBSCAN based on computational geometry, Machine Learning with Applications 6 (2021) 100148. https://doi.org/10.1016/j.mlwa.2021.100148.
[26] D. Zhu, ILD-BOOST: An Enhanced Outlier Detection Model Combining iForest, LOF, and DBSCAN on Spark, Proceedings of the 2025 2nd International Conference on Computer Network and Cloud Computing. 2025. (2025) 70-

75. https://doi.org/10.1145/3744451.3744462.
[27] F. Pourkamali-Anaraki, T. Nasrin, R.E. Jensen, A.M. Peterson, C.J. Hansen, Evaluation of classification models in limited data scenarios with application to additive manufacturing, Engineering Applications of Artificial Intelligence 126 (2023) 106983. https://doi.org/10.1016/j.engappai.2023.106983.
[28] D. Fullington, E. Yangue, M.M. Bappy, C. Liu, W. Tian, Leveraging small-scale datasets for additive manufacturing process modeling and part certification: Current practice and remaining gaps, Journal of Manufacturing Systems 75 (2024) 306-321. https://doi.org/10.1016/j.jmsy.2024.04.021.
[29] C. Cooper, J. Zhang, J. Huang, J. Bennett, J. Cao, R.X. Gao, Tensile strength prediction in directed energy deposition through physics-informed machine learning and Shapley additive explanations, Journal of Materials Processing Technology 315 (2023) 117908. https://doi.org/10.1016/j.jmatprotec.2023.117908.
[30] R. De Maesschalck, D. Jouan-Rimbaud, D.L. Massart, The mahalanobis distance, Chemometrics and intelligent laboratory systems 50(1) (2000) 1-18. https://doi.org/10.1016/S0169-7439(99)00047-7.
[31] D. Shetve, R. VaraPrasad, R. Trestian, H.X. Nguyen, H. Venkataraman, Cats: Cluster-aided two-step approach for anomaly detection in smart manufacturing, Advances in Computing and Network Communications: Proceedings of CoCoNet 2020, Volume 2 (2021) 103-115. https://doi.org/10.1007/978-981-33-6987-0_9.
[32] R. Rakhi, S.K. Tripathi, B. Gupta, S.S. Lamba, ODMN: A hybrid approach for outlier detection using mutual neighbors: Rakhi R. et al, Signal, Image and Video Processing 19(12) (2025) 1011. https://doi.org/10.1007/s11760-025-04602-w.
[33] D. Muhr, M. Affenzeller, Little data is often enough for distance-based outlier detection, Procedia Computer Science 200 (2022) 984-992. https://doi.org/10.1016/j.procs.2022.01.297.
[34] A. Adesh, G. Shobha, J. Shetty, L. Xu, Local outlier factor for anomaly detection in HPCC systems, Journal of Parallel and Distributed Computing 192 (2024) 104923. https://doi.org/10.1016/j.jpdc.2024.104923.
[35] A.H. Abuzaid, Identifying density-based local outliers in medical multivariate circular data, Statistics in medicine 39(21) (2020) 2793-2798. https://doi.org/10.1002/sim.8576.
[36] R.S. Stroud, A. Al-Saffar, M. Carter, M.P. Moody, S. Pedrazzini, M.R. Wenman, Testing Outlier Detection Algorithms for Identifying Early Stage Solute Clusters in Atom Probe Tomography, Microscopy and Microanalysis 30(5) (2024) 853-865. https://doi.org/10.1093/mam/ozae076.
[37] Z. Qi, J. Zhang, X. Chen, X. Qi, Comparative study of neighbor-based methods for local outlier detection, Journal of Ambient Intelligence and Smart Environments 17(4) (2025) 494-515. https://doi.org/10.1177/18761364251359900.
[38] Z. Gu, S. Sharma, D.A. Riley, M.V. Pantawane, S.S. Joshi, S. Fu, N.B. Dahotre, A universal predictor-based machine learning model for optimal process maps in laser powder bed fusion process, Journal of Intelligent Manufacturing 34(8) (2023) 3341-3363. https://doi.org/10.1007/s10845-022-02004-0.
[39] L. Zhu, J. Wang, Z. Song, H. Guo, B. Li, Y. Liu, Research on Density Prediction of Laser Powder Bed Fusion Process Parameters for IN718 Nickel-Based Superalloy Based on Machine Learning, Materials 19(12) (2026) 2455. https://doi.org/10.3390/ma19122455.
[40] A. Whitt, R. Seede, J. Ye, M. Elverud, M. Vaughan, A. Elwany, R. Arroyave, I. Karaman, A process optimization framework for laser direct energy deposition: Densification, microstructure, and mechanical properties of an FeCr alloy, Journal of Manufacturing Processes 85 (2023) 434-449. https://doi.org/10.1016/j.jmapro.2022.11.028.
[41] Niu Jingyi, Lu Siwei, Zhang Beining, Yang Chuncheng, Li DIchen, Study on the Effectiveness of Machine Learning Algorithms for Process Parameter Prediction in 3D Printing Process of Variable-component Composites, Journal of Mechanical Engineering 60(21) (2024) 263-274. https://doi.org/10.3901/JME.2024.21.263.
[42] J. Grünewald, K. Wudy, Dimensionless process windows in laser-based powder bed fusion of AISI 316L using ring-shaped beam profiles, Additive Manufacturing Letters 14 (2025) 100284. https://doi.org/10.1016/j.addlet.2025.100284.
[43] B. Gao, S. Peng, T. Li, F. Wang, J. Guo, C. Liu, H. Zhang, Integration of improved meta-heuristic and machine learning for optimizing energy efficiency in additive manufacturing process, Energy 306 (2024) 132518. https://doi.org/10.1016/j.energy.2024.132518.

[44] D.R. Feenstra, A. Molotnikov, N. Birbilis, Utilisation of artificial neural networks to rationalise processing windows in directed energy deposition applications, Materials & Design 198 (2021) 109342. https://doi.org/10.1016/j.matdes.2020.109342.
[45] A.K. Singh, Y. Mundada, P. Bajaj, M.B. Wilms, J.P. Patil, S.K. Mishra, E.A. Jägle, A. Arora, Investigation of temperature distribution and solidification morphology in multilayered directed energy deposition of Al-0.5 Sc-0.5 Si alloy, International Journal of Heat and Mass Transfer 186 (2022) 122492. https://doi.org/10.1016/j.ijheatmasstransfer.2021.122492.
[46] J. Zheng, C. Liu, S. Huang, Y. He, A novel adaptive dynamic GA combined with AM to optimize ANN for multi-output prediction: Small samples enhanced in industrial processing, Information Sciences 644 (2023) 119285. https://doi.org/10.1016/j.ins.2023.119285.

Supplementary Files

This is a list of supplementary files associated with this preprint. Click to download.

- DatasetSample5065marked.png
- Datasetsample5065nomark.png
- DatasetSample66100marked.jpg
- DatasetSample125marked.jpg
- DatasetSample2649marked.jpg
- DatasetSample2649nomark.jpg
- DatasetSample125nomark.jpg
- Datasetsample66100nomark.jpg